Unsupervised Co-Learning on $\mathcal{G}$-Manifolds Across Irreducible Representations

Yifeng Fan[1] **Tingran Gao**[2] **Zhizhen Zhao**[1]
[1]University of Illinois at Urbana-Champaign   [2]University of Chicago
{yifengf2, zhizhenz}@illinois.edu   tingrangao@galton.uchicago.edu

Abstract

We introduce a novel co-learning paradigm for manifolds naturally admitting an action of a transformation group $\mathcal{G}$, motivated by recent developments on learning a manifold from attached fibre bundle structures. We utilize a representation theoretic mechanism that canonically associates multiple independent vector bundles over a common base manifold, which provides multiple views for the geometry of the underlying manifold. The consistency across these fibre bundles provide a common base for performing unsupervised manifold co-learning through the redundancy created artificially across irreducible representations of the transformation group. We demonstrate the efficacy of our proposed algorithmic paradigm through drastically improved robust nearest neighbor identification in cryo-electron microscopy image analysis and the clustering accuracy in community detection.

1 Introduction

Fighting with the *curse of dimensionality* by leveraging low-dimensional intrinsic structures has become an important guiding principle in modern data science. Apart from classical structural assumptions commonly employed in sparsity or low-rank models in high dimensional statistics [63, 11, 12, 49, 2, 64, 67], recently it has become of interest to leverage more intricate properties of the underlying geometric model, motivated by algebraic or differential geometry techniques, for efficient learning and inference from massive complex datasets [15, 16, 44, 46, 8]. The assumption that high dimensional datasets lie approximately on a low-dimensional manifold, known as the *manifold hypothesis*, has been the cornerstone for the development of manifold learning [62, 52, 18, 3, 4, 5, 17, 57, 66] in the past few decades.

In many real applications, the low-dimensional manifold underlying the dataset of high ambient dimensionality admits additional structures that can be fully leveraged to gain deeper insights into the geometry of the data. One class of such examples arises in scientific fields such as *cryo-electron microscopy* (cryo-EM), where large numbers of random projections for a three-dimensional molecule generate massive collections of images that can be determined only up to in-plane rotations [59, 72]. Another source of examples is the application in computer vision and robotics, where a major challenge is to recognize and compare three-dimensional spatial configurations up to the action of Euclidean or conformal groups [28, 10]. In these examples, the dataset of interest consists of images or shapes of potentially high spatial resolution, and admits a natural group action $g \in \mathcal{G}$ that plays the role of a nuisance or latent variable that needs to be "quotient out" before useful information is revealed.

In geometric terms, on top of a differentiable manifold $\mathcal{M}$ underlying the dataset of interest, as assumed in the manifold hypothesis, we also assume the manifold admits a smooth *right action* of a Lie group $\mathcal{G}$, in the sense that there is a smooth map $\phi : \mathcal{G} \times \mathcal{M} \to \mathcal{M}$ satisfying $\phi(e, m) = m$ and $\phi(g_2, \phi(g_1, m)) = \phi(g_1 g_2, m)$ for all $m \in \mathcal{M}$ and $g_1, g_2 \in \mathcal{G}$, where e is the identity element of $\mathcal{G}$. A *left action* can be defined similarly. Such a group action reflects abundant information about the symmetry of the underlying manifold, with which one can study geometric and topological

properties of the underlying manifold through the lens of the orbit, stabilized, or induced finite- or infinite-dimensional representations of $\mathcal{G}$. In modern differential and symplectic geometry literature, a smooth manifold $\mathcal{M}$ admitting the action of a Lie group $\mathcal{G}$ is often referred to as a $\mathcal{G}$-**manifold** (see e.g. [40, §6], [50, 1, 33] and references therein), and this transformation-centered methodology has been proven fruitful [42, 53, 40, 30] by several generations of geometers and topologists.

Recent development of manifold learning has started to digest and incorporate the additional information encoded in the $\mathcal{G}$-actions on the low-dimensional manifold underlying the high-dimensional data. In [36], the authors constructed a *steerable graph Laplacian* on the manifold of images — modeled as a rotationally invariant manifold (or U (1)-manifold in geometric terms) — that serves the role of graph Laplacian in manifold learning but with naturally built-in rotational invariance by construction. In [38], the authors proposed a principal bundle model for image denoising, which achieved state-of-the-art performance by combining patch-based image analysis with rotationally invariant distances in microscopy [47]. A major contribution of this paper is to provide deeper insights into the success of these group-transformation-based manifold learning techniques from the perspective of *multi-view learning* [56, 60, 37] or *co-training* [7], and propose a family of new methods that systematically utilize these additional information in a systematic way, by exploiting the inherent consistency across representation theoretic patterns. Motivated by the recent line of research bridging manifold learning with principal and associated fibre bundles [57, 58, 22, 20, 19], we point out that to a $\mathcal{G}$-manifold admitting a principal bundle structure is naturally associated as many vector bundles as the number of distinct irreducible representations of the transformation group $\mathcal{G}$, and each of these vector bundles provide a separate "view" towards unveiling the geometry of the common *base manifold* on which all the fibre bundles reside.

Specifically, the main contributions of this paper are summarized as follows: (1) We propose a new unsupervised co-learning paradigm on $\mathcal{G}$-manifold and propose an optimal alignment affinity measure for high-dimensional data points that lie on or close to a lower dimensional $\mathcal{G}$-manifold, using both the local cycle consistency of group transformations on the manifold (graph) and the algebraic consistency of the unitary irreducible representations of the transformations; (2) We introduce the invariant moments affinity in order to bypass the computationally intensive pairwise optimal alignment search and efficiently learn the underlying local neighborhood structure; and (3) We empirically demonstrate that our new framework is extremely robust to noise and apply it to improve cryo-EM image analysis and the clustering accuracy in community detection. Code is available on `https://github.com/frankfyf/G-manifold-learning`.

2   Related Work

Manifold Learning: After the ground-breaking works of [62, 52], [5, 56, 41] provided reproducing kernel Hilbert space frameworks for scalar and vector valued kernel and interpreted the manifold assumption as a specific type of regularization; [3, 4, 14] used the estimated eigenfunctions of the Laplace–Beltrami operator to parametrize the underlying manifold; [24, 25, 59] investigated into the representation theoretic pattern of an integral operator acting on certain complex line bundles over the unit two-sphere naturally arising from cryo-EM image analysis; [57, 58, 22] demonstrated the benefit of using differential operators defined on fibre bundles over the manifold, instead of the Laplace–Beltrami operator on the manifold itself, in manifold learning tasks. Recently, [20, 19, 23] proposed to utilize the consistency across multiple irreducible representations of a compact Lie group to improve spectral decomposition based algorithms.

Co-training and Multi-view Learning: In their seminal work [7], Blum and Mitchell demonstrated both in theory and in practice that distinct "views" of a dataset can be combined together to improve the performance of learning tasks, through their complementary yet consistent prediction for unlabelled data. Similar ideas exploiting the consistency of the information contained in different sets of features has long existed in statistical literature such as canonical correlation analysis [29]. Since then, multi-view learning has remained a powerful idea percolating through aspects of machine learning ranging from supervised and semi-supervised learning to active learning and transfer learning [21, 43, 61, 13, 55, 56, 34, 35]. See surveys [60, 69, 70, 37] for more detailed accounts.

3   Geometric Motivation

We first provide a brief overview of the key concepts used in this paper from elementary group representation theory. Interested readers are referred to [54, 9] for more details.

Groups and Representation: A *group* $\mathcal{G}$ is a set with an operation $\mathcal{G} \times \mathcal{G} \to \mathcal{G}$ obeying the following axioms: (1) $\forall g_1, g_2 \in \mathcal{G}, g_1 g_2 \in \mathcal{G}$; (2) $\forall g_1, g_2, g_3 \in \mathcal{G}, g_1(g_2 g_3) = (g_1 g_2) g_3$; (3) There is a unique $e \in \mathcal{G}$ called the *identity* of $\mathcal{G}$, such that $eg = ge = g, \forall g \in \mathcal{G}$; (4) $\forall g \in \mathcal{G}$, there is a corresponding element $g^{-1} \in \mathcal{G}$ called the *inverse* of g, such that $gg^{-1} = g^{-1} g = e$. A $d_\rho \times d_\rho$-dimensional *representation* of a group $\mathcal{G}$ over a field $\mathbb{F}$ is a matrix valued function $\rho : \mathcal{G} \to \mathbb{F}^{d_\rho \times d_\rho}$ such that $\rho(g_1)\rho(g_2) = \rho(g_1 g_2), \forall g_1, g_2 \in \mathcal{G}$. In this paper, we assume $\mathbb{F} = \mathbb{C}$. A representation ρ is said to be *unitary* if $\rho(g^{-1}) = \rho(g)^*$ for any $g \in \mathcal{G}$ and ρ is said to be *reducible* if it can be decomposed into a direct sum of lower-dimensional representations as $\rho(g) = Q^{-1}(\rho_1(g) \bigoplus \rho_2(g))Q$ for some invertible matrix $Q \in \mathbb{C}^{d_\rho \times d_\rho}$, otherwise ρ is *irreducible*, the symbol $\bigoplus$ denotes the direct sum. For a compact group, there exists a complete set of *inequivalent irreducible representations (**in brevity: irreps**)* and any representation can be reduced into a direct sum of irreps.

Fourier Transform: In many applications of interest, the Lie group is compact and thus always admits irreps, and the concept of irreps allows generalizing the Fourier transform to any compact group. By the renowned Peter–Weyl theorem, any square integrable function $f \in L_2(\mathcal{G})$ can be decomposed as

$$f(g) = \sum_{k=0}^{\infty} d_k \mathrm{Tr}\,[F_k \rho_k(g)], \quad \text{and} \quad F_k = \int_{\mathcal{G}} f(g)\rho_k^*(g)d\mu_g, \tag{1}$$

where each $\rho_k : \mathcal{G} \to \mathbb{C}^{d_k \times d_k}$ is a *unitary irrep* of $\mathcal{G}$ with dimension $d_k \in \mathbb{N}$. This is the compact Lie group analogy of the standard Fourier series over the unit circle. The *"generalized Fourier coefficient"* F_k in (1) is defined by the integral taken with respect to the Haar measure on $\mathcal{G}$.

Motivation: Motivated by [38, 36], we consider the principal bundle structures on a $\mathcal{G}$-manifold $\mathcal{M}$. Below we state the definitions of fibre bundle and principal bundle for convenience; see [6] for more details. Briefly speaking, a fibre bundle is a manifold which is locally diffeomorphic to a product space, and a principal fibre bundle is a fibre bundle with a natural group action on its "fibres."

Definition 1 (Fibre Bundle) *Let $\mathcal{M}, \mathcal{B}, \mathcal{F}$ be three differentiable manifolds, and let $\pi : \mathcal{M} \to \mathcal{B}$ denote a smooth surjective map between $\mathcal{M}$ and $\mathcal{B}$. We say that $\mathcal{M} \xrightarrow{\pi} \mathcal{B}$ (or just $\mathcal{M}$ for short) is a **fibre bundle** with typical fibre $\mathcal{F}$ over $\mathcal{B}$ if $\mathcal{B}$ admits an open cover $\mathscr{U}$ such that $\pi^{-1}(U)$ is diffeomorphic to product space $U \times \mathcal{F}$ for any open set $U \in \mathcal{U}$. For any $x \in \mathcal{B}$, we denote $\mathcal{F}_x := \pi^{-1}(x)$ and call it the **fibre** over x.*

Definition 2 (Principal Bundle) *Let $\mathcal{M}$ be a fibre bundle, and $\mathcal{G}$ a Lie group. We call $\mathcal{M}$ a **principal $\mathcal{G}$-bundle** if (1) $\mathcal{M}$ is a fibre bundle, (2) $\mathcal{M}$ admits a right action of $\mathcal{G}$ that preserves the fibres of $\mathcal{M}$, in the sense that for any $m \in \mathcal{M}$ we have $\pi(m) = \pi(g \cdot m)$, and (3) For any two points $p, q \in \mathcal{M}$ on the same fibre of $\mathcal{M}$, there exists a group element $g \in \mathcal{G}$ satisfying $p \cdot g = q$.*

If $\mathcal{M}$ is a principal $\mathcal{G}$-bundle over $\mathcal{B}$, any representation ρ of $\mathcal{G}$ on a vector space V induces an **associated vector bundle** over $\mathcal{B}$ with typical fibre V, denoted as $\mathcal{M} \times_\rho V$, defined as a quotient space $\mathcal{M} \times_\rho V := \mathcal{M} \times V / \sim$ where the equivalence relation is defined by $(m \cdot g, v) \sim (m, \rho(g)v)$ for all $m \in \mathcal{M}$, $g \in \mathcal{G}$, and $v \in V$. This construction gives rise to as many different associated vector bundles as the number of distinct representations of the Lie group $\mathcal{G}$. This allows us to study the $\mathcal{G}$-manifold $\mathcal{M}$, as a principal $\mathcal{G}$-bundle, through tools developed for learning an unknown manifold from attached vector bundle structures, such as *vector diffusion maps* (VDM) [57, 58]. We consider each of these associated vector bundles as a distinct "view" towards the unknown data manifold $\mathcal{M}$, as the representations inducing these vector bundles are different. In the rest of this paper, we will illustrate with several examples how to design learning and inference algorithms that exploit the inherent consistency in these associated vector bundles by representation theoretic machinery. Unlike the co-training setting where the consistency is induced from the labelled samples onto the unlabelled samples, in our unsupervised setting no labelled training data is provided and the consistency is induced purely from the geometry of the $\mathcal{G}$-manifold.

4   Methods

Problem Setup: Given a collection of n data points $\{x_1, \ldots, x_n\} \subset \mathbb{R}^l$, we assume they lie on or close to a low dimensional smooth manifold $\mathcal{M}$ of intrinsic dimension $d \ll l$, and that $\mathcal{M}$ is a $\mathcal{G}$-*manifold* admitting the structure of a principal $\mathcal{G}$-bundle with a compact Lie group $\mathcal{G}$. The data space $\mathcal{M}$ is closed under the action of $\mathcal{G}$. That is, $g \cdot x \in \mathcal{M}$ for all group transformations $g \in \mathcal{G}$ and

data points $x \in \mathcal{M}$, where '·' denotes the group action. As an example, in a cryo-EM image dataset each image is a projection of a macromolecule with a random orientation, therefore $\mathcal{M} = \mathrm{SO}(3)$, which is the 3-D rotation group, $\mathcal{G} = \mathrm{SO}(2)$ which is the in-plane rotation of images. The $\mathcal{G}$-*invariant distance* d_{ij} between two data points x_i and x_j is defined as

$$d_{ij} = \min_{g \in \mathcal{G}} \|x_i - g \cdot x_j\|, \quad \text{and} \quad g_{ij} = \arg\min_{g \in \mathcal{G}} \|x_i - g \cdot x_j\|. \tag{2}$$

where $\|\cdot\|$ is the Euclidean distance on the ambient space $\mathbb{R}^l$ and g_{ij} is the associated alignment which is assumed to be unique. Then we build an undirected graph $G = (V, E)$ whose nodes are represented by data points, edge connection is given based on d_{ij} using the ϵ-neighborhood criterion, i.e. $(i, j) \in E$ iff $d_{ij} <= \epsilon$, or κ-nearest neighbor criterion, i.e. $(i, j) \in E$ iff j is one of the κ nearest neighbors of i. The edge weights w_{ij} are defined using a kernel function on d_{ij} as $w_{ij} = K_\sigma(d_{ij})$. The resulting graph G is defined on the quotient space $\mathcal{B} := \mathcal{M}/\mathcal{G}$ and is invariant to the group transformations g_{ij} within data points, e.g. for the viewing angles of cryo-EM images $\mathcal{B} = \mathrm{SO}(3)/\mathrm{SO}(2) = \mathrm{S}^2$. In a noiseless world, G should be a neighborhood graph which only connects data points on $\mathcal{B}$ with small d_{ij}. However, in many applications, noise in the observational data severely degrades the estimations of $\mathcal{G}$-invariant distances d_{ij} and optimal alignments g_{ij}. This leads to errors in the edge connection of G, which connect distant data points on $\mathcal{B}$ where their underlying geodesic distances are large.

Given the noisy graph, we consider the problem of *removing the wrong connections* and *recovering the underlying clean graph structure on* $\mathcal{B}$, especially under high level of noise. We propose a robust, unsupervised co-learning framework for addressing this, it has two steps which first builds a series of adjacency matrices with different irreps and filters the original noisy graph as denoising, further it checks the affinity between node pairs for identifying true neighbors in the clean graph. The main intuition is to *systematically explores the consistency* of the group transformation of the principal bundles across all irreps of $\mathcal{G}$, results in a robustness measurement of the affinity (see Fig. 1).

Weight Matrices Using Irreps: We start from building a series of weight matrices using multiple irreps of the compact Lie group $\mathcal{G}$. Given the graph $G = (V, E)$ with n nodes and the group transformations $g \in \mathcal{G}$, we assign weight on each edge $(i, j) \in E$ by taking into account both the scalar edge connection weight w_{ij} and the associated alignment g_{ij} using unitary irreps ρ_k for $k = 1, \ldots, k_{\max}$. The resulting graph can be described by a set of weight matrices W_k:

Figure 1: Illustration of our co-learning paradigm: Given a graph with irreps ρ_k for $k = 1, \ldots, k_{\max}$, we identify neighbors by investigating the following consistencies: Within each graph of a single irrep ρ_k, if nodes i, j and s are neighbors, the cycle consistency of the group transformation holds: $\rho_k(g_{js})\rho_k(g_{si})\rho_k(g_{ij}) \approx I_{d_k \times d_k}$; Across different irreps, if i, j are neighbors, the transformation g_{ij} should be consistent algebraically (along the orange lines connecting the blue dots).

$$W_k(i, j) = \begin{cases} w_{ij} \rho_k(g_{ij}) & (i, j) \in E \\ 0 & \text{otherwise} \end{cases} \tag{3}$$

where $w_{ij} = w_{ji}$ and $\rho_k(g_{ji}) = \rho_k^*(g_{ij})$ for all $(i, j) \in E$. Recall the unitary irrep $\rho_k(g_{ij}) \in \mathbb{C}^{d_k \times d_k}$ is a $d_k \times d_k$ matrix, therefore W_k is a block matrix with $n \times n$ blocks of size $d_k \times d_k$. In particular, the corresponding degree matrix D_k is also a block diagonal matrix with the (i, i)-block $D_k(i, i)$ as:

$$D_k(i, i) = \deg(i) I_{d_k \times d_k}, \quad \deg(i) := \sum\nolimits_{j:(i,j) \in E} w_{ij}. \tag{4}$$

The Hilbert space $\mathcal{H}$, as a unitary representation of the compact Lie group $\mathcal{G}$, admits an isotypic decomposition $\mathcal{H} = \bigoplus \mathcal{H}_k$, where a function f is in $\mathcal{H}_k$ if and only if $f(xg) = g^k f(x)$. Then for each irrep ρ_k, we construct a normalized matrix $A_k = D_k^{-1} W_k$, which is an *averaging operator* for vector fields in $\mathcal{H}_k$. That is, for any vector $z_k \in \mathcal{H}_k$:

$$(A_k z_k)(i) = \frac{1}{\deg(i)} \sum\nolimits_{j:(i,j) \in E} w_{ij} \rho_k(g_{ij}) z_k(j). \tag{5}$$

Notice that A_k is similar to a Hermitian matrix $\widetilde{A}_k$ as:

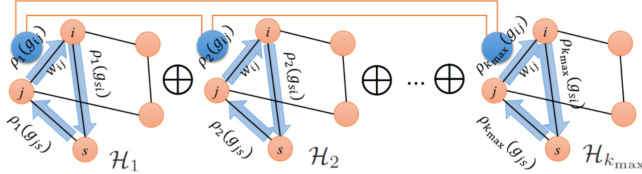$$\widetilde{A}_k = D_k^{1/2} A_k D_k^{-1/2} = D_k^{-1/2} W_k D_k^{-1/2} \tag{6}$$

4

Algorithm 1: Weight Matrices Filtering

Input: Initial graph $G = (V, E)$ with n nodes, for each $(i, j) \in E$ the scalar weight w_{ij} and alignment g_{ij}, maximum frequency $k_{\max}$, cutoff parameter m_k for $k = 1, \dots, k_{\max}$, and spectral filter η_t

Output: The filtered weight matrices $\widetilde{W}_{k,t}$ for $k = 1, \dots, k_{\max}$

---

1   **for** $k = 1, \dots, k_{\max}$ **do**

2   Construct the block weight matrix W_k of size $nd_k \times nd_k$ in (3) and the normalized symmetric matrix $\widetilde{A}_k$ in (6)

3   Compute the largest $m_k d_k$ eigenvalues $\lambda_1^{(k)} \geq \lambda_2^{(k)}, \geq, \dots, \geq \lambda_{m_k d_k}^{(k)}$ of $\widetilde{A}_k$ and the corresponding eigenvectors $\{u_l^{(k)}\}_{l=1}^{m_k d_k}$

4   **for** $i = 1, \dots, n$ **do**

5   Construct the $\mathcal{G}$-equivariant mapping, $\psi_t^{(k)} : i \mapsto \left[\eta_t(\lambda_1)^{1/2} u_1^{(k)}(i), \dots, \eta_t(\lambda_{m_k})^{1/2} u_{m_k d_k}^{(k)}(i) \right]$

6   (Optional) Compute the SVD of $\psi_t^{(k)}(i) = U \Sigma V^*$ and the normalized mapping $\widetilde{\psi}_t^{(k)}(i) = U V^*$.

7   **end**

8   Vertically concatenate $\widetilde{\psi}_t^{(k)}(i)$ or $\psi_t^{(k)}(i)$ to form the matrix $\Psi_t^{(k)}$ of size $nd_k \times m_k d_k$

9   Construct the filtered and normalized weight matrix $\widetilde{W}_{k,t} = \Psi_t^{(k)} \left(\Psi_t^{(k)} \right)^*$.

10 **end**

---

which has real eigenvalues and orthonormal eigenvectors $\{\lambda_l^{(k)}, u_l^{(k)}\}_{l=1}^{nd_k}$, and all the eigenvalues are within $[-1, 1]$. For simplicity, we assume data points are uniformly distributed on $\mathcal{B}$. If not, the normalization proposed in [17] can be applied to W_k. Now suppose there is a random walk on G with a transition matrix A_0 and the trivial representations $\rho_0(g) = 1, \forall g \in \mathcal{G}$, then $A_0^{2t}(i, j)$ is the transition probability from i to j with $2t$ steps. Due to the usage of $\rho_0(g_{ij})$, $A_0^{2t}(i, j)$ not only takes into account the connectivity between the nodes i and j, but also checks the consistency of transformations along all length-$2t$ paths between i and j. Generally, in other cases when $k \geq 1$, $A_k^{2t}(i, j)$ is a sub-block matrix which still encodes such consistencies. Intuitively if i, j are true neighbors on G, their transformations should be in agreement and we expect $\|A_k^{2t}(i, j)\|_{\text{HS}}^2$ or $\|\widetilde{A}_k^{2t}(i, j)\|_{\text{HS}}^2$ to be large, where $\| \cdot \|_{\text{HS}}$ is the Hilbert-Schmidt norm. Previously, *vector diffusion maps* (VDM) [57, 58] considers $k = 1$ and defines the pairwise affinity as $\|\widetilde{A}_1^{2t}(i, j)\|_{\text{HS}}^2$.

Weight Matrices Filtering: For denoising the graph, we generalize the VDM framework by first computing the filtered and normalized weight matrix $\widetilde{W}_{k,t} = \eta_t(\widetilde{A}_k)$ for all irreps ρ_k's, where $\eta_t(\cdot)$ denotes a spectral filter acting on the eigenvalues, for example $\eta_t(\lambda) = \lambda^{2t}$ as VDM. Moreover, since the small eigenvalues of $\widetilde{A}_k$ are more sensitive to noise, a truncation is applied by only keeping the top $m_k d_k$ eigenvalues and eigenvectors. Specifically, we equally divide $u_l^{(k)}$ of length nd_k into n blocks and denote the ith block as $u_l^{(k)}(i)$. In this way, we define a $\mathcal{G}$-*equivariant mapping* as:

$$ \psi_t^{(k)} : i \mapsto \left[\eta_t(\lambda_1)^{1/2} u_1^{(k)}(i), \dots, \eta_t(\lambda_{m_k d_k})^{1/2} u_{m_k d_k}^{(k)}(i) \right] \in \mathbb{C}^{d_k \times m_k d_k}, \quad i = 1, 2, \dots, n. \quad (7) $$

It can be further normalized to ensure the diagonal blocks of $\widetilde{W}_{k,t}$ are identity matrices, i.e. $\widetilde{W}_{k,t}(i, i) = I_{d_k \times d_k}$ for all nodes i. The steps for weight matrices filtering are detailed in Alg. 1. The resulting denoised $\widetilde{W}_{k,t}$ is then used for building our affinity measures.

Optimal Alignment Affinity: At each irrep ρ_k, the filtered $\widetilde{W}_{k,t}$ involves the transformation consistency of the graph represented by W_k and has its own ability to measure the affinity. Then similar to the unsupervised multi-view learning approach, it is advantageous to boost this by coupling the information under different irreps and to achieve a more accurate measurement (see Fig. 1). Furthermore, notice that if i and j are true neighbors, for each irrep ρ_k the block $\widetilde{W}_{k,t}(i, j)$ should encode the same amount of associated alignment g_{ij}. Therefore, by applying the algebraic relation among $\widetilde{W}_{k,t}$ across all irreps, we define the *optimal alignment affinity* according to the generalized Fourier transform in (1) and the definition of the weight matrices in (3):

$$ S_t^{\text{OA}}(i, j) := \max_{g \in \mathcal{G}} \frac{1}{k_{\max}} \left| \sum_{k=1}^{k_{\max}} \text{Tr} \left[\widetilde{W}_{k,t}(i, j) \rho_k^*(g) \right] \right|, \quad (8) $$

which can be evaluated using generalized FFTs [39]. Here both the cycle consistency within each graph and the algebraic relation across different irreps in Fig. 1 are considered.

Power Spectrum Affinity: Searching for the optimal alignment among all transformations as above could be computationally challenging and extremely time consuming. Therefore, invariant features can be used to speed up the computation. First we consider the *power spectrum*, which is the Fourier transform of the auto-correlation defined as $P_f(k) = F_k F_k^*$ according to the convolution theorem. It is transformation invariant since under the right action of $g \in \mathcal{G}$, the Fourier coefficients $F_k \to F_k \rho_k(g)$ and $P_{f \cdot g}(k) = F_k \rho_k(g) \rho_k(g)^* F_k^* = P_f(k)$. Hence, for each k we compute the power spectrum P_k of $\widetilde{W}_{k,t}$ and combine them as the *power spectrum affinity*:

$$S_t^{\text{power spec}}(i,j) = \frac{1}{k_{\max}} \sum_{k=1}^{k_{\max}} \text{Tr}\left[P_k(i,j)\right], \quad \text{with } P_k(i,j) = \widetilde{W}_{k,t}(i,j)\widetilde{W}_{k,t}(i,j)^*, \tag{9}$$

which does not require the search of optimal alignment and is thus computationally efficient. Recently, multi-frequency vector diffusion maps (MFVDM) [20] considers $\mathcal{G} = \text{SO}(2)$ and sums the power spectrum at different irreps as their affinity. Here, we extend it to a general compact Lie group.

Bispectrum Affinity: Although, the power spectrum affinity combines the information at different irreps, it does not couple them and loses the *relative phase information*, i.e. the transformation across different irreps ρ_k (see Fig. 1). Consequently, the affinity might be inaccurate under high level of noise. In order to systematically impose the algebraic consistency without solving the optimization problem in (8), we consider another invariant feature called *bispectrum*, which is the Fourier transform of the triple correlation and has been used in several fields [32, 27, 72, 31]. Formally, let us consider two unitary irreps ρ_{k_1} and ρ_{k_2} on finite dimensional vector spaces $\mathcal{H}_{k_1}$ and $\mathcal{H}_{k_2}$ of the compact Lie group $\mathcal{G}$. There is a unique decomposition of $\rho_{k_1} \bigotimes \rho_{k_2}$ into a set of unitary irreps ρ_k, $k \in \mathbb{N}$, where $\bigotimes$ is the Kronecker product of matrices, and we use $\bigoplus$ to denote direct sum. There exists $\mathcal{G}$-equivariant maps from $\mathcal{H}_{k_1} \bigotimes \mathcal{H}_{k_2} \to \bigoplus \mathcal{H}_k$, called generalized *Clebsch–Gordan* coefficients C_{k_1,k_2} for $\mathcal{G}$, which satisfies:

$$\rho_{k_1}(g) \bigotimes \rho_{k_2}(g) = C_{k_1,k_2} \left[\bigoplus_{k \in k_1 \otimes k_2} \rho_k(g) \right] C_{k_1,k_2}^*. \tag{10}$$

Using (10) and the fact that C_{k_1,k_2} and ρ_k's are unitary matrices, we have

$$\left[\rho_{k_1}(g) \bigotimes \rho_{k_2}(g)\right] C_{k_1,k_2} \left[\bigoplus_{k \in k_1 \otimes k_2} \rho_k^*(g) \right] C_{k_1,k_2}^* = I_{d_{k_1} d_{k_2} \times d_{k_1} d_{k_2}}. \tag{11}$$

Particularly, the triple correlation of a function f on $\mathcal{G}$ can be defined as $a_{3,f}(g_1,g_2) = \int_{\mathcal{G}} f^*(g)f(gg_1)f(gg_2)d\mu_g$. Then the bispectrum is defined as the Fourier transform of $a_{3,f}$ as

$$B_f(k_1,k_2) = \left[F_{k_1} \bigotimes F_{k_2}\right] C_{k_1,k_2} \left[\bigoplus_{k \in k_1 \otimes k_2} F_k^* \right] C_{k_1,k_2}^*. \tag{12}$$

Under the action of g, we have the following properties of the Fourier coefficients of f: (1) $F_k \to F_k \rho_k(g)$, and (2) $F_{k_1} \bigotimes F_{k_2} \to (F_{k_1}\rho_{k_1}(g)) \bigotimes (F_{k_1}\rho_{k_1}(g)) = (F_{k_1} \bigotimes F_{k_1})(\rho_{k_1}(g) \bigotimes \rho_{k_2}(g))$. Therefore, B_f is $\mathcal{G}$-invariant according to (11) and (12). By combining the bispectrum at different k_1 and k_2, we establish the *bispectrum affinity* as,

$$S_t^{\text{bispec}}(i,j) = \frac{1}{k_{\max}^2} \left| \sum_{k_1=1}^{k_{\max}} \sum_{k_2=1}^{k_{\max}} \text{Tr}\left[B_{k_1,k_2,t}(i,j)\right] \right|, \quad \text{with} \tag{13}$$

$$B_{k_1,k_2,t}(i,j) = \left[\widetilde{W}_{k_1,t}(i,j) \bigotimes \widetilde{W}_{k_2,t}(i,j)\right] C_{k_1,k_2} \left[\bigoplus_{k \in k_1 \otimes k_2} \widetilde{W}_{k,t}^*(i,j) \right] C_{k_1,k_2}^*. \tag{14}$$
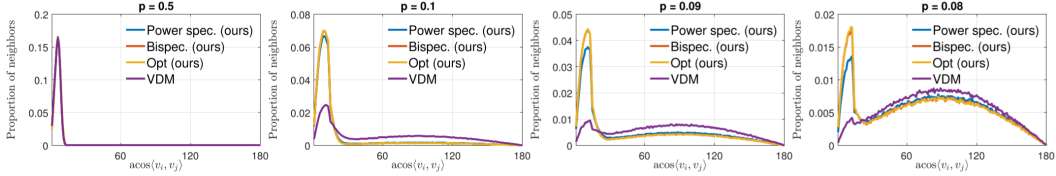
6

Figure 2: Histograms of $\arccos \langle v_i, v_j \rangle$ between estimated nearest neighbors on $\mathcal{M} = \mathrm{SO}(3)$, $\mathcal{G} = \mathrm{SO}(2)$ and $\mathcal{B} = \mathrm{S}^2$ with different SNRs. The clean histogram should peak at small angles. The lines of the bispectrum and the optimal alignment affinities almost overlap in all these plots. We set $k_{\max} = 6$, $m_k = 10$ for all k's and $t = 1$.

If the transformations are consistent across different k's, the trace of $B_{k_1,k_2,t}$ in (14) should be large. Therefore, this affinity not only takes into account the consistency of the transformation at each irrep, but also explores the algebraic consistency across different irreps.

Higher Order Invariant Moments: The power spectrum and bispectrum are second-order and third-order cumulants, certainly it is possible to design affinities by using higher order invariant features. For example, we can define the order-$d + 1$ $\mathcal{G}$-invariant features as: $M_{k_1,\ldots,k_d} = [F_{k_1} \bigotimes \cdots \bigotimes F_{k_d}] C_{k_1,\ldots,k_d} \left[\bigoplus_{k \in k_1 \otimes \cdots \otimes k_d} F_k^* \right] C_{k_1,\ldots,k_d}^*$, where $C_{k_1,\ldots,k_d}$ is the extension of the Clebsch–Gordan coefficients. However, using higher order spectra dramatically increases the computational complexity. In practice, the bispectrum is sufficient to check the consistency of the group transformations between nodes and across all irreps.

Computational Complexity: Filtering the normalized weight matrix involves computing the top $m_k d_k$ eigenvectors of the sparse Hermitian matrices A_k, for $k = 1, \ldots, k_{\max}$, which can be efficiently evaluated using block Lanczos method [51], and its cost is $O(nm_k d_k^2 (m_k + l_k))$, where l_k is the average number of non-zero elements in each row of $\widetilde{A}_k$. We compute the spectral decomposition for different k's in parallel. Computing the power spectrum invariant affinity for all pairs takes $O(n^2 \sum_{k=1}^{k_{\max}} d_k^2)$ flops. The computational complexity of evaluating the bispectrum invariant affinity is $O(n^2 (\sum_{k_1=0}^{k_{\max}} \sum_{k_2=0}^{k_{\max}} d_{k_1}^2 d_{k_2}^2))$. For the optimal alignment affinity, the computational complexity depends on the cost of optimal alignment search C_a and the total cost is $O(n^2 C_a)$. For certain group structures, where FFTs are developed, the optimal alignment affinity can be efficiently and accurately approximated. However, C_a is still larger than the computation cost of invariants.

Examples with $\mathcal{G} = \mathrm{SO}(2)$ and $\mathrm{SO}(3)$: If the group transformation is 2-D in-plane rotation, i.e. $\mathcal{G} = \mathrm{SO}(2)$, the unitary irreps will be $\rho_k(\alpha) = e^{ik\alpha}$, where $\alpha \in (0, 2\pi]$ is the rotation angle. The dimensions of the irreps are $d_k = 1$, and $k_1 \bigotimes k_2 = k_1 + k_2$. The generalized Clebsch–Gordan coefficients is 1 for all (k_1, k_2) pairs. If $\mathcal{G}$ is the 3-D rotation group, i.e. $\mathcal{G} = \mathrm{SO}(3)$, the unitary irreps are the Wigner D-matrices for $\omega \in \mathrm{SO}(3)$ [68]. The dimensions of the irreps are $d_k = 2k + 1$, and $k_1 \bigotimes k_2 = \{|k_1 - k_2|, \ldots, k_1 + k_2\}$. The Clebsch–Gordan coefficients for all (k_1, k_2) pairs can be numerically precomputed [26]. These two classical examples are frequently used in the real world and are investigated in our experiments.

5 Experiments

We evaluate our paradigm through three examples: (1) Nearest neighbor (In brevity: **NN**) search on 2-sphere S^2 with $\mathcal{G} = \mathrm{SO}(2)$; (2) nearest viewing angle search for cryo-EM images; (3) spectral clustering with $\mathcal{G} = \mathrm{SO}(2)$ or $\mathcal{G} = \mathrm{SO}(3)$ transformation. We compare with the baseline vector diffusion maps (VDM) [57]. In particular, since the greatest advantage of our paradigm is the robustness to noise, we demonstrate this through datasets contaminated by extremely high level of noise. The setting of hyper parameters, e.g. $k_{\max}$ and m_k, are shown in the captions, we point out that our algorithm is not sensitive to the choice of parameters. The experiments are conducted in MATLAB on a computer with Intel i7 7th generation quad core CPU.

NN Search for $\mathcal{M} = \mathrm{SO}(3)$, $\mathcal{G} = \mathrm{SO}(2)$, $\mathcal{B} = \mathrm{S}^2$: We simulate $n = 10^4$ points uniformly distributed over $\mathcal{M} = \mathrm{SO}(3)$ according to the Haar measure. Each point can be represented by a 3×3 orthogonal matrix $R = [R^1, R^2, R^3]$, whose determinant is equal to 1. Then the vector $v = R^3$ can be realized as a point on the unit 2-sphere (i.e. $\mathcal{B} = \mathrm{S}^2$). The first two columns R^1 and R^2 spans the tangent plane of the sphere at v. Given two points i and j, there exists a rotation angle α_{ij} that
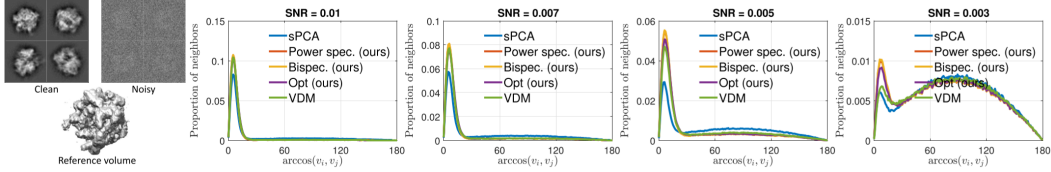
Figure 3: Nearest viewing angle search for cryo-EM images. *Left*: clean, noisy (SNR = 0.01) projections image samples, and reference volume of 70s ribosome; *Right*: Histograms of $\arccos \langle v_i, v_j \rangle$ between estimated nearest neighbors. sPCA is the initial noisy input of our graph structure. The lines of power spectrum and bispectrum almost overlap in all these plots. We set $k_{\max} = 20$, $m_k = 20$ for all k's and $t = 1$.

optimally aligns the tangent bundles $[R_j^1, R_j^2]$ to $[R_i^1, R_i^2]$ as in (2). Therefore, the manifold $\mathcal{M}$ is a $\mathcal{G}$-manifold with $\mathcal{G} = \mathrm{SO}(2)$. Then we build a clean neighborhood graph $G = (V, E)$ by connecting nodes with $\langle v_i, v_j \rangle \geq 0.97$, and add noise following a *random rewiring model* [59]. With probability p, we keep the existing edge $(i, j) \in E$. With probability $1 - p$, we remove it and link i to another vertex drawn uniformly at random from the remaining vertices that are not already connected to i. For those rewired edges, their alignments are uniformly distributed over $[0, 2\pi]$ according to the Haar measure. In this way, the probability p controls the signal to noise ratio (SNR) where $p = 1$ indicates the clean case, while $p = 0$ is fully random. For each node, we identify its 50 NNs based on the three proposed affinities and the affinity in VDM. In Fig. 2 we plot the histogram of $\arccos \langle v_i, v_j \rangle$ of identified NNs under different SNRs. When $p = 0.08$ to $p = 0.1$ (over 90% edges are corrupted), bispectrum and optimal alignment achieve similar result and outperform power spectrum and VDM. This indicates our proposed affinities are able to recover the underlying clean graph, even at an extremely high noise level.

Nearest Viewing Angle Search for Cryo-EM Images: One important application of the NN search above is in *cryo-EM image analysis*. Given a series of projection images of a macromolecule with unknown random orientations and extremely low SNR (see Fig. 3), we aim to identify images with similar projection directions and perform local rotational alignment, then image SNR can be boosted by averaging the aligned images. Therefore, each projection image can be viewed as a point lying on the 2-sphere (i.e. $\mathcal{B} = \mathrm{S}^2$), and the group transformation is the in-plane rotation of an image (i.e., $\mathcal{G} = \mathrm{SO}(2)$).

In our experiments, we simulate $n = 10^4$ projection images from a 3D electron density map of the 70S ribosome, the orientations of all projections are uniformly distributed over $\mathrm{SO}(3)$ and the images are contaminated by additive white Gaussian noise (see Fig. 3 for noisy samples). As preprocessing, we build the initial graph G by using fast steerable PCA (sPCA) [71] and rotationally invariant features [72] to initially identify the images of similar views and the corresponding in-plane rotational alignments. Similar to the example above, we compute the affinities for NNs identification. In Fig. 3, we display the histograms of $\arccos \langle v_i, v_j \rangle$ of identified NNs under different SNRs. Result shows that all proposed affinities outperform VDM. The power spectrum and the bispectrum affinities achieve similar result, and outperform the optimal alignment affinity. This result is different from the previous example with the random rewiring model on S^2. This is because those two examples have different noise model, the random rewiring model has independent noise on edges, whereas the examples using cryo-EM images have independent noise on nodes with dependent noise on edges.

Spectral Clustering with $\mathrm{SO}(2)$ or $\mathrm{SO}(3)$ Transformations: We apply our framework to spectral clustering. In particular, we assume there exists a group transformation $g_{ij} \in \mathcal{G}$ in addition to the scalar weight w_{ij} between members (nodes) in a network. Formally, given n data points with K equal sized clusters, for each point i, we uniformly assign an in-plane rotational angle $\alpha_i \in [0, 2\pi)$, or a 3-D rotation $\omega_i \in \mathrm{SO}(3)$. Then the optimal alignment is $\alpha_{ij} = \alpha_i - \alpha_j$, or $\omega_{ij} = \omega_i \omega_j^{-1}$. We build the clean graph by fully connecting nodes within each cluster. The noisy graph is then built following the random rewiring model with a rewiring probability p. We perform clustering by using our proposed affinities as the input of spectral clustering, and compare with the traditional spectral clustering [45, 65] which only takes into account the scalar edge connection, and VDM [57], which defines affinity based on the transformation consistency at a single representation. In Tab. 1, we use *Rand index* [48] to measure the performance (larger value is better). Our three affinities achieve similar accuracy and they outperform the traditional spectral clustering (scalar) and VDM. The results reported in Tab. 1 are evaluated over 50 trials for $\mathrm{SO}(2)$ and 10 trials for $\mathrm{SO}(3)$ respectively.

8

Table 1: Rand index (larger value is better) of spectral clustering results with SO(2) or SO(3) group transformation. We set the number of clusters *Left*: $K = 2$ and *right*: $K = 10$. For $K = 10$ and SO(3) case, each cluster has 25 points, otherwise each cluster has 50 points. We set $m_k = K$, $k_{\max} = 10$ and $t = 1$ for all cases.

$\mathcal{G}$	method	$K = 2$ clusters			$K = 10$ clusters		
		$p = 0.16$	$p = 0.20$	$p = 0.25$	$p = 0.16$	$p = 0.20$	$p = 0.25$
SO(2)	Scalar	0.569 ± 0.069	0.705 ± 0.092	0.837 ± 0.059	0.868 ± 0.010	0.948 ± 0.015	0.981 ± 0.013
	VDM	0.526 ± 0.036	0.644 ± 0.076	0.857 ± 0.057	0.892 ± 0.010	0.963 ± 0.011	0.994 ± 0.008
	Power spec. (ours)	0.670 ± 0.065	0.899 ± 0.051	0.981 ± 0.021	0.975 ± 0.010	0.991 ± 0.011	0.998 ± 0.006
	Opt (ours)	$\mathbf{0.687 \pm 0.011}$	$\mathbf{0.912 \pm 0.009}$	$\mathbf{0.986 \pm 0.007}$	$\mathbf{0.976 \pm 0.012}$	0.994 ± 0.008	0.997 ± 0.005
	Bispec. (ours)	0.664 ± 0.073	0.901 ± 0.062	0.983 ± 0.019	0.967 ± 0.014	$\mathbf{0.997 \pm 0.003}$	$\mathbf{1 \pm 0}$
SO(3)	Scalar	0.572 ± 0.061	0.666 ± 0.095	0.862 ± 0.056	0.838 ± 0.003	0.838 ± 0.007	0.909 ± 0.019
	VDM	0.600 ± 0.048	0.840 ± 0.056	0.974 ± 0.023	0.850 ± 0.011	0.919 ± 0.013	0.965 ± 0.014
	Power spec. (ours)	$\mathbf{0.921 \pm 0.038}$	0.986 ± 0.016	$\mathbf{1 \pm 0}$	$\mathbf{0.874 \pm 0.011}$	0.939 ± 0.011	$\mathbf{0.981 \pm 0.017}$
	Bispec. (ours)	0.911 ± 0.043	$\mathbf{0.990 \pm 0.010}$	$\mathbf{1 \pm 0}$	0.869 ± 0.012	$\mathbf{0.943 \pm 0.009}$	0.979 ± 0.011

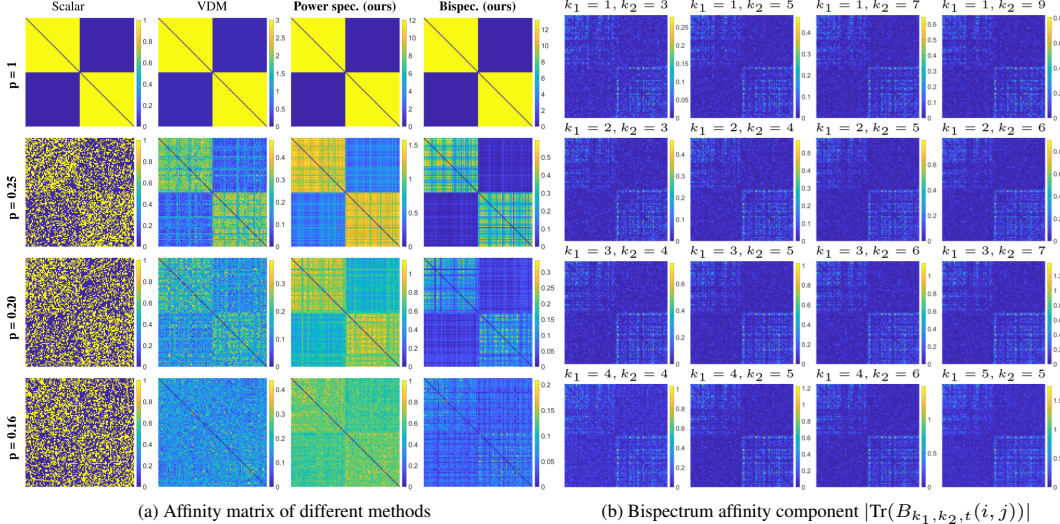(a) Affinity matrix of different methods   (b) Bispectrum affinity component $|\mathrm{Tr}(B_{k_1,k_2,t}(i,j))|$

Figure 4: Spectral clustering for $K = 2$ clusters with SO(3) group transformation. The underlying clean graph is corrupted according to the random rewiring model. *Left*: Plot of the affinity matrix by different approaches. The clusters are of equal size and form two diagonal blocks in the clean affinity matrix (see the *scalar* column at $p = 1$). Here we do not include the affinity of each node with itself and the diagonal entries are 0; *Right*: Plot of the bispecturm affinity $|\mathrm{Tr}\left[B_{k_1,k_2,t}(i,j)\right]|$ at different $k_1, k_2, p = 0.16$.

For a better understanding, we visualize the $n \times n$ affinity matrices by different approaches as shown in Fig. 4a at $K = 2$ and $\mathcal{G} = \mathrm{SO}(3)$. We observe that at high noise levels, such as $p = 0.16$ or 0.2, the underlying 2-cluster structure is visually easier to be identified through our proposed affinities. In particular, as the bispectrum affinity in (13) is the combination of the bispectrum coefficients $B_f(k_1, k_2)$, Fig. 4b shows the component $|\mathrm{Tr}\left[B_{k_1,k_2,t}(i,j)\right]|$ at different k_1, k_2. Visually, the 2-cluster structure appears in each (k_1, k_2) component with some variations across different components. Combining those information together results in a more robust classifier.

6   Conclusion

In this paper, we propose a novel mathematical and computational framework for unsupervised co-learning on $\mathcal{G}$-manifolds across multiple unitary irreps for robust nearest neighbor search and spectral clustering. We have a two stage algorithm: At the first stage, the graph adjacency matrices are individually denoised through spectral filtering. This step uses the local cycle consistency of the group transformation; The second stage checks the algebraic consistency over different irreps and we propose three different ways to combine the information across all irreps. Using invariant moments bypasses the pairwise alignment and is computationally more efficient than the affinity based on the optimal alignment search. Experimental results show the efficacy of the framework compared to the state-of-the-art methods, which do not take into account of the transformation group or only use a single representation.

References

[1] Andrey V. Alekseevsky and Dmitry V. Alekseevsky. Riemannian G-manifold with one-dimensional orbit space. *Annals of global analysis and geometry*, 11(3):197–211, 1993.

[2] Derek Bean, Peter J. Bickel, Noureddine El Karoui, and Bin Yu. Optimal M-estimation in high-dimensional regression. *Proceedings of the National Academy of Sciences*, 110(36):14563–14568, 2013.

[3] Mikhail Belkin and Partha Niyogi. Laplacian eigenmaps and spectral techniques for embedding and clustering. In *NIPS*, 2002.

[4] Mikhail Belkin and Partha Niyogi. Laplacian eigenmaps for dimensionality reduction and data representation. *Neural computation*, 2003.

[5] Mikhail Belkin, Partha Niyogi, and Vikas Sindhwani. Manifold regularization: A geometric framework for learning from labeled and unlabeled examples. *Journal of machine learning research*, 7(Nov):2399–2434, 2006.

[6] Nicole Berline, Ezra Getzler, and Michèle Vergne. *Heat Kernels and Dirac Operators (Grundlehren Text Editions)*. Springer, 1992 edition, 12 2003.

[7] Avrim Blum and Tom Mitchell. Combining labeled and unlabeled data with co-training. In *Proceedings of the eleventh annual conference on Computational learning theory*, pages 92–100. ACM, 1998.

[8] Paul Breiding, Sara Kališnik, Bernd Sturmfels, and Madeleine Weinstein. Learning algebraic varieties from samples. *Revista Matemática Complutense*, 31(3):545–593, 2018.

[9] Theodor Bröcker and Tammo Tom Dieck. *Representations of compact Lie groups*, volume 98. Springer Science & Business Media, 2013.

[10] Alexander Bronstein, Michael Bronstein, and Ron Kimmel. *Numerical Geometry of Non-Rigid Shapes*. Springer Publishing Company, Incorporated, 1 edition, 2008.

[11] Emmanuel J Candès and Benjamin Recht. Exact matrix completion via convex optimization. *Foundations of Computational mathematics*, 9(6):717, 2009.

[12] Venkat Chandrasekaran, Sujay Sanghavi, Pablo A Parrilo, and Alan S Willsky. Sparse and low-rank matrix decompositions. *IFAC Proceedings Volumes*, 42(10):1493–1498, 2009.

[13] Minmin Chen, Kilian Q. Weinberger, and John C. Blitzer. Co-training for domain adaptation. In *Proceedings of the 24th International Conference on Neural Information Processing Systems*, NIPS'11, pages 2456–2464, USA, 2011. Curran Associates Inc.

[14] Ronald R Coifman and Stéphane Lafon. Diffusion maps. *Applied and computational harmonic analysis*, 21(1):5–30, 2006.

[15] Ronald R Coifman, Stephane Lafon, Ann B Lee, Mauro Maggioni, Boaz Nadler, Frederick Warner, and Steven W Zucker. Geometric diffusions as a tool for harmonic analysis and structure definition of data: diffusion maps. *Proceedings of the National Academy of Sciences of the United States of America*, 102(21):7426–31, may 2005.

[16] Ronald R Coifman, Stephane Lafon, Ann B Lee, Mauro Maggioni, Boaz Nadler, Frederick Warner, and Steven W Zucker. Geometric diffusions as a tool for harmonic analysis and structure definition of data: multiscale methods. *Proceedings of the National Academy of Sciences of the United States of America*, 102(21):7432–7, may 2005.

[17] Ronald R. Coifman and Stéphane Lafon. Diffusion Maps. *Applied and Computational Harmonic Analysis*, 21(1):5–30, 2006. Special Issue: Diffusion Maps and Wavelets.

[18] David L. Donoho and Carrie Grimes. Hessian Eigenmaps: Locally Linear Embedding Techniques for High-Dimensional Data. *Proceedings of the National Academy of Sciences*, 100(10):5591–5596, 2003.

[19] Yifeng Fan and Zhizhen Zhao. Cryo-electron microscopy image analysis using multi-frequency vector diffusion maps. *arXiv preprint arXiv:1904.07772*, 2019.

[20] Yifeng Fan and Zhizhen Zhao. Multi-frequency vector diffusion maps. In *ICML*, 2019.

[21] Jason Farquhar, David Hardoon, Hongying Meng, John S. Shawe-Taylor, and Sándor Szedmák. Two view learning: SVM-2K, theory and practice. In Y. Weiss, B. Schölkopf, and J. C. Platt, editors, *Advances in Neural Information Processing Systems 18*, pages 355–362. MIT Press, 2006.

[22] Tingran Gao. The diffusion geometry of fibre bundles: Horizontal diffusion maps. *arXiv preprint arXiv:1602.02330*, 2016.

[23] Tingran Gao and Zhizhen Zhao. Multi-frequency phase synchronization. In *ICML*, 2019.

[24] Ronny Hadani and Amit Singer. Representation Theoretic Patterns in Three Dimensional Cryo-Electron Microscopy I: The Intrinsic Reconstitution Algorithm. *Annals of Mathematics*, 174(2):1219–1241, 2011.

[25] Ronny Hadani and Amit Singer. Representation theoretic patterns in three-dimensional cryo-electron microscopy II – the class averaging problem. *Foundations of Computational Mathematics*, 11(5):589–616, 2011.

[26] Brian Hall. *Lie groups, Lie algebras, and representations: an elementary introduction*, volume 222. Springer, 2015.

[27] Ramakrishna Kakarala and Dansheng Mao. A theory of phase-sensitive rotation invariance with spherical harmonic and moment-based representations. In *2010 IEEE Computer Society Conference on Computer Vision and Pattern Recognition*, pages 105–112. IEEE, 2010.

[28] David G. Kendall. A survey of the statistical theory of shape. *Statist. Sci.*, 4(2):87–99, 05 1989.

[29] Jon R Kettenring. Canonical analysis of several sets of variables. *Biometrika*, 58(3):433–451, 12 1971.

[30] Shoshichi Kobayashi. *Transformation groups in differential geometry*. Springer Science & Business Media, 2012.

[31] Imre Risi Kondor. *Group theoretical methods in machine learning*. PhD thesis, Columbia University, 2008.

[32] Risi Kondor. A novel set of rotationally and translationally invariant features for images based on the non-commutative bispectrum. *arXiv preprint cs/0701127*, 2007.

[33] Risi Kondor and Shubhendu Trivedi. On the generalization of equivariance and convolution in neural networks to the action of compact groups. In *International Conference on Machine Learning*, pages 2752–2760, 2018.

[34] Abhishek Kumar and Hal Daume III. A co-training approach for multi-view spectral clustering. In *Proceedings of the 28th International Conference on International Conference on Machine Learning*, ICML'11, pages 393–400, USA, 2011. Omnipress.

[35] Abhishek Kumar, Piyush Rai, and Hal Daume. Co-regularized multi-view spectral clustering. In J. Shawe-Taylor, R. S. Zemel, P. L. Bartlett, F. Pereira, and K. Q. Weinberger, editors, *Advances in Neural Information Processing Systems 24*, pages 1413–1421. Curran Associates, Inc., 2011.

[36] Boris Landa and Yoel Shkolnisky. The steerable graph laplacian and its application to filtering image datasets. *SIAM Journal on Imaging Sciences*, 11(4):2254–2304, 2018.

[37] Yingming Li, Ming Yang, and Zhongfei Mark Zhang. A survey of multi-view representation learning. *IEEE Transactions on Knowledge and Data Engineering*, pages 1–1, 2018.

[38] Chen-Yun Lin, Arin Minasian, Xin Jessica Qi, and Hau-Tieng Wu. Manifold learning via the principle bundle approach. *Frontiers in Applied Mathematics and Statistics*, 4:21, 2018.

[39] David K Maslen and Daniel N Rockmore. Generalized FFTs—a survey of some recent results. In *Groups and Computation II*, volume 28, pages 183–287. American Mathematical Soc., 1997.

[40] Peter W Michor. *Topics in differential geometry*, volume 93. American Mathematical Soc., 2008.

[41] Hà Quang Minh, Loris Bazzani, and Vittorio Murino. A unifying framework in vector-valued reproducing kernel hilbert spaces for manifold regularization and co-regularized multi-view learning. *Journal of Machine Learning Research*, 17(25):1–72, 2016.

[42] David Mumford, John Fogarty, and Frances Kirwan. *Geometric invariant theory*, volume 34. Springer Science & Business Media, 1994.

[43] Ion Muslea, Steven Minton, and Craig A. Knoblock. Active learning with multiple views. *J. Artif. Int. Res.*, 27(1):203–233, October 2006.

[44] Boaz Nadler, Stephane Lafon, Ioannis Kevrekidis, and Ronald R Coifman. Diffusion maps, spectral clustering and eigenfunctions of Fokker-Planck operators. In *Advances in neural information processing systems*, pages 955–962, 2006.

[45] Andrew Y. Ng, Michael I. Jordan, and Yair Weiss. On spectral clustering: Analysis and an algorithm. In *Advances in neural information processing systems*, pages 849–856, 2002.

[46] Greg Ongie, Rebecca Willett, Robert D. Nowak, and Laura Balzano. Algebraic variety models for high-rank matrix completion. In Doina Precup and Yee Whye Teh, editors, *Proceedings of the 34th International Conference on Machine Learning*, volume 70 of *Proceedings of Machine Learning Research*, pages 2691–2700, International Convention Centre, Sydney, Australia, 06–11 Aug 2017. PMLR.

[47] Pawel A Penczek, Jun Zhu, and Joachim Frank. A common-lines based method for determining orientations for $n > 3$ particle projections simultaneously. *Ultramicroscopy*, 63(3-4):205–218, 1996.

[48] William M Rand. Objective criteria for the evaluation of clustering methods. *Journal of the American Statistical association*, 66(336):846–850, 1971.

[49] Garvesh Raskutti, Martin J Wainwright, and Bin Yu. Minimax-optimal rates for high-dimensional sparse additive models over kernel classes. *Journal of Machine Learning Research*, 13:281–319, 2012.

[50] Ken Richardson. The transverse geometry of g-manifolds and riemannian foliations. *Illinois Journal of Mathematics*, 45(2):517–535, 2001.

[51] Vladimir Rokhlin, Arthur Szlam, and Mark Tygert. A randomized algorithm for principal component analysis. *SIAM Journal on Matrix Analysis and Applications*, 31(3):1100–1124, 2009.

[52] Sam T. Roweis and Lawrence K. Saul. Nonlinear Dimensionality Reduction by Locally Linear Embedding. *Science*, 290(5500):2323–2326, 2000.

[53] Alexander HW Schmitt. *Geometric invariant theory and decorated principal bundles*, volume 11. European Mathematical Society, 2008.

[54] Jean-Pierre Serre. *Linear representations of finite groups*, volume 42. Springer, 1977.

[55] Vikas Sindhwani and Partha Niyogi. A co-regularized approach to semi-supervised learning with multiple views. In *Proceedings of the ICML Workshop on Learning with Multiple Views*, 2005.

[56] Vikas Sindhwani and David S. Rosenberg. An RKHS for multi-view learning and manifold co-regularization. In *Proceedings of the 25th international conference on Machine learning*, pages 976–983. ACM, 2008.

[57] Amit Singer and Hau-Tieng Wu. Vector diffusion maps and the connection Laplacian. *Communications on Pure and Applied Mathematics*, 65(8):1067–1144, 2012.

[58] Amit Singer and Hau-Tieng Wu. Spectral convergence of the connection Laplacian from random samples. *Information and Inference: A Journal of the IMA*, 6(1):58–123, 12 2016.

[59] Amit Singer, Zhizhen Zhao, Yoel Shkolnisky, and Ronny Hadani. Viewing angle classification of cryo-electron microscopy images using eigenvectors. *SIAM Journal on Imaging Sciences*, 4(2):723–759, 2011.

[60] Shiliang Sun. A survey of multi-view machine learning. *Neural Computing and Applications*, 23(7):2031–2038, Dec 2013.

[61] Shiliang Sun and David R. Hardoon. Active learning with extremely sparse labeled examples. *Neurocomputing*, 73(16):2980 – 2988, 2010. 10th Brazilian Symposium on Neural Networks (SBRN2008).

[62] Joshua B. Tenenbaum, Vin de Silva, and John C. Langford. A Global Geometric Framework for Nonlinear Dimensionality Reduction. *Science*, 290(5500):2319–2323, 2000.

[63] Robert Tibshirani, Martin Wainwright, and Trevor Hastie. *Statistical learning with sparsity: the lasso and generalizations*. Chapman and Hall/CRC, 2015.

[64] Roman Vershynin. *High-dimensional probability: An introduction with applications in data science*, volume 47. Cambridge University Press, 2018.

[65] Ulrike von Luxburg. A tutorial on spectral clustering. *Statistics and computing*, 17(4):395–416, 2007.

[66] Elif Vural and Christine Guillemot. A study of the classification of low-dimensional data with supervised manifold learning. *Journal of Machine Learning Research*, 18:1–55, 2018.

[67] Martin J. Wainwright. *High-dimensional statistics: A non-asymptotic viewpoint*, volume 48. Cambridge University Press, 2019.

[68] Eugene Paul Wigner. Gruppentheorie und ihre anwendung auf die quantenmechanik der atomspektren. *Monatshefte für Mathematik und Physik*, 39(1):A51, 1932.

[69] Chang Xu, Dacheng Tao, and Chao Xu. A survey on multi-view learning. *arXiv preprint arXiv:1304.5634*, 2013.

[70] Jing Zhao, Xijiong Xie, Xin Xu, and Shiliang Sun. Multi-view learning overview: Recent progress and new challenges. *Information Fusion*, 38:43 – 54, 2017.

[71] Zhizhen Zhao, Yoel Shkolnisky, and Amit Singer. Fast steerable principal component analysis. *IEEE transactions on computational imaging*, 2(1):1–12, 2016.

[72] Zhizhen Zhao and Amit Singer. Rotationally invariant image representation for viewing direction classification in cryo-EM. *Journal of structural biology*, 186(1):153–166, 2014.

Appendices

A Additional Results on Spectral Clustering

In the main paper, we visualize the $n \times n$ affinity matrices of $K = 2$ clusters with $\mathcal{G} = \mathrm{SO}(3)$ for spectral application, in the presence of edge noise. Here we provide another visualization of the affinity measures for the results in Table 1 of the main paper, with $K = 10$ and $\mathcal{G} = \mathrm{SO}(3)$. In Fig. 5, we show the affinity matrices using single frequency ($k = 1$) VDM, power spectrum, and bispectrum. The cutoff parameter m_k and maximum frequency $k_{\max}$ are set as $m_k = K = 10$ and $k_{\max} = 10$. We observe similar patterns for the 2-cluster example (see Fig. 4a in the main paper). For noisy examples with $p = 0.20$ and 0.16, the cluster structure is more easily identified through our proposed affinities compared to scalar edge weights used in the traditional spectral clustering [45], and frequency $k = 1$ VDM [57]. This again demonstrates the efficacy of our approach in estimating the cluster structures in the presence of large level of noise on edges.

Figure 5: Similarity measure for $K = 10$ clusters with $\mathrm{SO}(3)$ group transformation. The underlying clean graph is corrupted according to the random rewiring model. We show the plot of the affinity matrix by different approaches. The clusters are of equal size and form 10 diagonal blocks in the clean affinity matrix (see the *scalar* column at $p = 1$). Here we do not include the affinity of each node with itself and the diagonal entries are 0.

B Performance under Different Choices of Parameters

In this section, we include more numerical results to show the performance of our methods under different parameter settings and provide theoretical justification under a probabilistic model.

B.1 Nearest Neighbor Identification on Base Manifold

First, we analyze the spectral properties of the matrix W_k based on the random rewiring model [59]. Starting from the underlying true graph, we perturb the graph in the following way: with probability $1 - p$, we remove the clean edge $(i, j) \in E$ and create a link between i and some random vertex, drawn uniformly at random from the remaining vertices that are not connected to i. If the link between i and j is a rewired random link, then the associated group element g_{ij} is distributed over $\mathcal{G}$

according to the Haar measure. The corresponding matrix W_k is a random matrix under this model. If the distribution of g is the Haar measure on $\mathcal{G}$, we have $\mathbb{E}\rho_k(g) = 0_{d_k \times d_k}$ for $k \neq 0$. Therefore, we get $\mathbb{E}W_k = pW_k^{\text{clean}}$ for $k \neq 0$, where W_k^{clean} is the matrix with all links and group elements inferred correctly ($p = 1$). Thus the matrix W_k can be decomposed as,

$$W_k = pW_k^{\text{clean}} + R_k, \tag{15}$$

where R_k is a Hermitian random matrix with random blocks. The upper triangular part of the matrix contains independent random blocks with finite moments (the elements of R_k are all bounded). Thus we use p to describe the signal-to-noise ratio of the observed graph. According to the matrix perturbation theory, the top eigenvectors of W_k approximates the top eigenvectors of W_k^{clean} as long as the 2-norms of R_k is not too large.

We numerically test the sensitivity of our methods to the choice of parameters in application to the nearest neighbor identification on base manifold. The set up of the experiments is similar to Section 5 in the main paper. We simulate $n = 10^4$ data points uniformly sampled from $\mathcal{M} = \mathrm{SO}(3)$ and build the clean neighborhood graph on $\mathcal{B} = \mathrm{S}^2$. The random rewiring perturbation is then applied to the clean graph and the nearest neighbors are identified based on the proposed affinities, with two varying parameters: cutoff parameter m_k and maximum frequency $k_{\max}$. We evaluate by computing the proportion (in percentage) of all identified nearest neighbor pairs (i, j)'s whose $\langle v_i, v_j \rangle > 0.95$. The results are shown in Tab. 2 and Tab. 3. We have the following observation.

Cutoff Parameter m_k: Ideally, at each frequency k, the truncation cutoff m_k, that is, selecting the top $m_k d_k$ eigenvectors of matrix $\widetilde{A}_k = D_k^{-1/2} W_k D_k^{-1/2}$, should be set to include top eigenvectors that are not largely perturbed by noise and have nontrivial correlation with the eigenvectors of the clean matrix $\widetilde{A}_k^{\text{clean}}$. This value can vary between different frequencies. However, in practice, we set m_k to be a moderate constant for all k's. In all the trials, we set $k_{\max} = 10$. In Tab. 2, we observe that the accuracy is first improved when m_k increases since more information is included. However, the accuracy degrades or gets saturated when m_k is larger than a certain p dependent value due to the effects of noise. This implies a moderate m_k is needed for a trade-off between the useful information and the impact of noise.

Maximum Frequency $k_{\max}$: We test $k_{\max}$ from 2 to 100 and show the results in Tab. 3. We fix $m_k = 20$, when varying $k_{\max}$. In the extremely noisy cases, such as $p = 0.09$ and 0.10, the results improve when $k_{\max}$ increases within the range of the values we test. When $p > 0.1$, the accuracy first increases but then degrades or gets saturated after a certain p dependent value of $k_{\max}$. This indicates that the optimal choice of $k_{\max}$ depends on the noise level. Under this particular noise perturbation model, the higher the noise level is, the larger the $k_{\max}$ is needed. Also, since for all three proposed affinities the computation complexity greatly increase with a growing $k_{\max}$, it should be chosen that our computation budget can afford.

Table 2: The accuracy of nearest neighbor identification on base manifold with varying cutoff m_k for $\mathcal{M} = \mathrm{SO}(3), \mathcal{G} = \mathrm{SO}(2)$ and $\mathcal{B} = \mathrm{S}^2$. The maximum frequency is $k_{\max} = 10$ in all the experiments. We compute the proportion (in percentage) of identified neighbor pairs (i, j)'s whose $\langle v_i, v_j \rangle > 0.95$, at different signal-to-noise ratios p's. For each method we highlight its best result in boldface.

| p | method | Truncation cutoff m_k | | | | | |
		2	5	10	20	50	100
0.08	VDM	2.63	3.02	3.48	3.67	4.14	**4.59**
	Power spec. (ours)	2.91	4.71	5.93	7.05	9.16	**12.30**
	Opt (ours)	2.94	5.66	7.26	8.95	12.20	**16.43**
	Bispec. (ours)	2.88	5.53	7.24	8.70	11.91	**16.23**
0.09	VDM	2.82	4.60	8.05	**9.46**	9.25	9.13
	Power spec. (ours)	4.37	14.96	33.44	**38.85**	38.21	37.77
	Opt (ours)	5.64	22.65	45.70	**51.59**	50.93	49.77
	Bispec. (ours)	5.62	22.17	44.84	**50.44**	49.57	48.68
0.10	VDM	3.48	8.65	17.96	**27.56**	24.58	20.87
	Power spec. (ours)	8.29	38.22	68.09	**83.04**	78.92	73.56
	Opt (ours)	15.03	52.25	77.38	**87.72**	86.25	82.66
	Bispec. (ours)	14.95	51.19	76.57	**87.33**	85.56	81.90
0.5	VDM	57.04	98.48	99.99	**100**	**100**	**100**
	Power spec. (ours)	99.05	**100**	**100**	**100**	**100**	**100**
	Opt (ours)	99.60	99.99	**100**	**100**	**100**	**100**
	Bispec. (ours)	99.60	**100**	**100**	**100**	**100**	**100**

Table 3: The accuracy of nearest neighbor identification on base manifold with varying maximum frequency $k_{\max}$ for $\mathcal{M} = \mathrm{SO}(3)$, $\mathcal{G} = \mathrm{SO}(2)$ and $\mathcal{B} = \mathrm{S}^2$. The cutoff parameter is $m_k = 20$ in all the experiments. We compute the proportion (in percentage) of identified neighbor pairs (i, j)'s whose $\langle v_i, v_j \rangle > 0.95$, at different signal-to-noise ratios p's. For each method we highlight its best result in boldface. Note that VDM only uses single frequency $k_{\max} = 1$.

| p | method | Maximum frequency $k_{\max}$ | | | | |
		2	5	10	20	50
0.08	VDM			— 3.67 —		
	Power spec. (ours)	4.12	5.23	7.05	9.52	**11.45**
	Opt (ours)	4.06	5.39	8.95	16.59	**29.17**
	Bispec. (ours)	4.03	5.26	8.70	15.73	**26.55**
0.09	VDM			— 9.46 —		
	Power spec. (ours)	13.47	25.49	38.85	52.02	**55.40**
	Opt (ours)	13.28	29.74	51.59	71.21	**76.30**
	Bispec. (ours)	13.03	28.85	50.44	70.18	**77.26**
0.10	VDM			— 27.56 —		
	Power spec. (ours)	43.66	69.29	83.04	90.15	**90.56**
	Opt (ours)	43.42	73.69	87.72	**93.01**	92.07
	Bispec. (ours)	42.15	72.55	87.33	93.05	**93.20**
0.5	VDM			— 100 —		
	Power spec. (ours)	100	100	100	100	100
	Opt (ours)	100	100	100	100	100
	Bispec. (ours)	100	100	100	100	100

B.2 Spectral Clustering

We check the performance of our methods in spectral clustering under different parameter settings. From the clean cluster graph, we apply the random rewiring perturbation as described above.

Cutoff Parameter m_k: In the clean case, the number of non-zero eigenvalues of the weight matrices W_k is $d_k K$ for K clusters. Therefore, each W_k has a low-rank structure and so is the normalized Hermitian matrix $\widetilde{A}_k = D_k^{-1/2} W_k D_k^{-1/2}$. Then a truncation at top $d_k K$ eigenvectors (i.e. $m_k = K$) is enough for clustering. In the noise case, following the model in (15), we are still able to use the top $d_k K$ eigenvectors for clustering as long as the signal-to-noise ratio p is not too small. Using less eigenvectors as $m_k < K$ will lead to loss of information and using $m_k > K$ will include spurious information from noise. We conduct the experiments with $K = 10$ clusters, where each cluster contains 50 points, and $\mathcal{G} = \mathrm{SO}(2)$. We set $p = 0.16$, 0.2, 0.25 and $k_{\max} = 10$. We vary the cutoff m_k from 2 to 100 and display the Rand indices of the clustering results from different methods in Tab. 4. Tab. 4 shows that all of our proposed affinity measures achieve their best performance when $m_k \approx K$ and the performance degrades when m_k is too small or too large. We conclude that setting $m_k = K$ should be a good choice for spectral clustering.

Table 4: Spectral clustering accuracy with varying cutoff m_k: Rand index of spectral clustering results with $K = 10$ clusters, $\mathcal{G} = \mathrm{SO}(2)$ and $k_{\max} = 10$. Each cluster has 50 points. We run 10 trials for all results. For each method we highlight its best result in boldface.

| p | method | Truncation m_k | | | | | |
		2	5	10	20	50	100
0.16	Scalar	0.828 ± 0.032	0.847 ± 0.020	$\mathbf{0.865 \pm 0.017}$	0.853 ± 0.014	0.834 ± 0.010	0.823 ± 0.012
	VDM	0.825 ± 0.024	0.854 ± 0.021	0.879 ± 0.020	0.916 ± 0.015	$\mathbf{0.925 \pm 0.016}$	0.912 ± 0.019
	Power spec. (ours)	0.849 ± 0.022	0.938 ± 0.018	$\mathbf{0.979 \pm 0.008}$	0.961 ± 0.010	0.955 ± 0.012	0.973 ± 0.007
	Opt (ours)	0.878 ± 0.025	0.957 ± 0.016	0.966 ± 0.010	$\mathbf{0.983 \pm 0.007}$	0.960 ± 0.009	0.975 ± 0.008
	Bispec. (ours)	0.869 ± 0.019	0.948 ± 0.013	$\mathbf{0.975 \pm 0.009}$	0.955 ± 0.014	0.957 ± 0.008	0.927 ± 0.016
0.20	Scalar	0.838 ± 0.032	0.881 ± 0.024	$\mathbf{0.958 \pm 0.017}$	0.941 ± 0.010	0.845 ± 0.028	0.830 ± 0.031
	VDM	0.823 ± 0.027	0.903 ± 0.015	0.959 ± 0.011	0.958 ± 0.011	0.962 ± 0.008	$\mathbf{0.982 \pm 0.005}$
	Power spec. (ours)	0.894 ± 0.019	0.985 ± 0.007	$\mathbf{0.997 \pm 0.002}$	0.996 ± 0.002	0.996 ± 0.002	0.995 ± 0.003
	Opt (ours)	0.905 ± 0.020	0.993 ± 0.003	$\mathbf{0.998 \pm 0.001}$	0.996 ± 0.001	0.997 ± 0.001	0.974 ± 0.008
	Bispec. (ours)	0.895 ± 0.021	0.986 ± 0.07	$\mathbf{0.997 \pm 0.002}$	0.996 ± 0.002	0.964 ± 0.017	0.917 ± 0.024
0.25	Scalar	0.850 ± 0.016	0.913 ± 0.018	0.985 ± 0.018	$\mathbf{0.986 \pm 0.009}$	0.864 ± 0.032	0.830 ± 0.022
	VDM	0.854 ± 0.012	0.950 ± 0.011	0.992 ± 0.008	0.993 ± 0.005	$\mathbf{0.993 \pm 0.004}$	0.993 ± 0.005
	Power spec. (ours)	0.948 ± 0.021	0.998 ± 0.001	$\mathbf{1 \pm 0}$	$\mathbf{1 \pm 0}$	$\mathbf{1 \pm 0}$	$\mathbf{1 \pm 0}$
	Opt (ours)	0.982 ± 0.008	0.999 ± 0.001	$\mathbf{1 \pm 0}$	$\mathbf{1 \pm 0}$	$\mathbf{1 \pm 0}$	$\mathbf{1 \pm 0}$
	Bispec. (ours)	0.952 ± 0.013	0.998 ± 0.001	$\mathbf{1 \pm 0}$	$\mathbf{1 \pm 0}$	$\mathbf{1 \pm 0}$	$\mathbf{1 \pm 0}$

Maximum Frequency $k_{\mathbf{max}}$: We run another experiment with $K = 10$ clusters, $\mathcal{G} = \mathrm{SO}(2)$, and $m_k = 10$, with $p = 0.16, 0.2, 0.25$. Each cluster contains 50 points. We vary $k_{\max}$ from 2 to 100 and show the Rand indices of clustering results in Tab. 5. We observe that the accuracy gets improved with increasing $k_{\max}$ for all three proposed affinities. However, using a larger $k_{\max}$ increases the computational complexities for all three affinity measures and the dimension of the irrep might increase with k (e.g. the dimension of Wigner D-matrix at index k is $2k + 1$), which is undesirable. There is a trade-off between the statistical accuracy and computational complexity. Therefore, we use a moderate $k_{\max} = 10$ in the main paper.

Table 5: Spectral clustering accuracy with varying maximum frequency $k_{\max}$: Rand index of spectral clustering results with $K = 10$ clusters, $\mathcal{G} = \mathrm{SO}(2)$ and $m_k = 10$, each cluster has 50 points. We run 10 trials for all results. For each method we highlight the best result in boldface. Note that the scalar input and VDM are only for $k_{\max} = 0$ and $k_{\max} = 1$, respectively.

p	method	Maximum frequency $k_{\max}$					
		2	5	10	20	50	100
0.16	Scalar	— 0.865 ± 0 —					
	VDM	— 0.879 ± 0 —					
	Power spec. (ours)	0.920 ± 0.019	0.958 ± 0.009	0.979 ± 0.004	0.981 ± 0.004	0.965 ± 0.007	$\mathbf{0.985 \pm 0.003}$
	Opt (ours)	0.920 ± 0.014	0.951 ± 0.009	0.957 ± 0.008	0.988 ± 0.003	0.968 ± 0.005	$\mathbf{0.993 \pm 0.002}$
	Bispec. (ours)	0.898 ± 0.025	0.960 ± 0.010	0.975 ± 0.008	0.976 ± 0.007	0.989 ± 0.005	$\mathbf{0.990 \pm 0.004}$
0.20	Scalar	— 0.958 ± 0 —					
	VDM	— 0.959 ± 0 —					
	Power spec. (ours)	0.991 ± 0.003	0.974 ± 0.008	0.997 ± 0.001	0.997 ± 0.001	0.999 ± 0.001	$\mathbf{1 \pm 0}$
	Opt (ours)	0.970 ± 0.012	0.996 ± 0.002	0.998 ± 0.001	0.998 ± 0.001	$\mathbf{0.999 \pm 0.001}$	$\mathbf{0.999 \pm 0.001}$
	Bispec. (ours)	0.989 ± 0.005	0.996 ± 0.002	0.997 ± 0.001	0.998 ± 0.001	$\mathbf{1 \pm 0}$	$\mathbf{1 \pm 0}$
0.25	Scalar	— 0.985 ± 0 —					
	VDM	— 0.992 ± 0 —					
	Power spec. (ours)	0.997 ± 0.001	$\mathbf{1 \pm 0}$	$\mathbf{1 \pm 0}$	$\mathbf{1 \pm 0}$	$\mathbf{1 \pm 0}$	$\mathbf{1 \pm 0}$
	Opt (ours)	0.998 ± 0.001	$\mathbf{1 \pm 0}$	$\mathbf{1 \pm 0}$	$\mathbf{1 \pm 0}$	$\mathbf{1 \pm 0}$	$\mathbf{1 \pm 0}$
	Bispec. (ours)	0.996 ± 0.002	$\mathbf{1 \pm 0}$	$\mathbf{1 \pm 0}$	$\mathbf{1 \pm 0}$	$\mathbf{1 \pm 0}$	$\mathbf{1 \pm 0}$